

Article

A MOF-Mediated Strategy for In Situ Niobium Doping and Synthesis of High-Performance Single-Crystal Ni-Rich Cathodes

Yinkun Gao, Huazhang Zhou, Shumin Liu, Shuyun Guan, Mingyang Liu, Peng Gao, Yongming Zhu and Xudong Li *

Department of Applied Chemistry, Harbin Institute of Technology at Weihai, Weihai 264209, China; 23s130266@stu.hit.edu.cn (Y.G.); zhouhz2024@126.com (H.Z.); 23s030052@stu.hit.edu.cn (S.L.); gsyyyun@163.com (S.G.); 24s030036@stu.hit.edu.cn (M.L.); gaofei5075@sina.com (P.G.); zymhit@hit.edu.cn (Y.Z.)

* Correspondence: lixdong@hit.edu.cn

Abstract

The development of single-crystal Ni-rich layered cathode materials (SC-NCMs) is regarded as an effective strategy to address the mechanical failure issues commonly associated with polycrystalline counterparts. However, the industrial production of SC-NCM faces challenges such as lengthy processing steps, high manufacturing costs, and inconsistent product quality. In this study, we innovatively propose a metal/organic framework (MOF)-mediated one-step synthesis strategy to achieve controllable structural preparation and in situ Nb⁵⁺ doping in SC-NCM. Using a Ni–Co–Mn-based MOF as both precursor and self-template, we precisely regulated the thermal treatment pathway to guide the nucleation and oriented growth of high-density SC-NCM particles. Simultaneously, Nb⁵⁺ was pre-anchored within the MOF framework, enabling atomic-level homogeneous doping into the transition metal layers during crystal growth. Exceptional electrochemical performance is revealed in the in situ Nb-doped SC-NCM, with an initial discharge capacity reaching 176 mAh/g at a 1C rate and a remarkable capacity retention of 86.36% maintained after 200 cycles. This study paves a versatile and innovative pathway for the design of high-stability, high-energy-density cathode materials via a MOF-mediated synthesis strategy, enabling precise manipulation of both morphology and chemical composition.



Academic Editor: Hirotoshi Yamada

Received: 12 September 2025

Revised: 1 October 2025

Accepted: 3 October 2025

Published: 5 October 2025

Citation: Gao, Y.; Zhou, H.; Liu, S.; Guan, S.; Liu, M.; Gao, P.; Zhu, Y.; Li, X. A MOF-Mediated Strategy for In Situ Niobium Doping and Synthesis of High-Performance Single-Crystal Ni-Rich Cathodes. *Batteries* **2025**, *11*, 368. <https://doi.org/10.3390/batteries11100368>

Copyright: © 2025 by the authors. Licensee MDPI, Basel, Switzerland. This article is an open access article distributed under the terms and conditions of the Creative Commons Attribution (CC BY) license (<https://creativecommons.org/licenses/by/4.0/>).

Keywords: lithium-ion battery; single-crystal; Ni-rich cathode material; metal/organic framework; in situ doping

1. Introduction

In recent decades, the surge of electric vehicles has driven a paradigm shift in energy storage markets, with lithium-ion batteries (LIBs) establishing themselves as the cornerstone technology within the electrochemical domain. This dominance is rooted in intrinsic technical virtues: superior cyclability minimizing capacity degradation across repeated charge cycles, negligible fade rates over prolonged operation, and high operational potentials enabling voltage-efficient energy conversion [1–3]. In particular, the pursuit of higher energy density and longer cycle life has driven extensive research into advanced cathode materials [4–7]. Among these, SC-NCM have attracted considerable attention due to their superior structural stability compared to polycrystalline counterparts [8–11]. The absence of grain boundaries in single-crystal particles effectively mitigates microcrack formation and irreversible phase transitions during prolonged cycling, thereby improving capacity retention and safety [12–15]. Consequently, SC-NCM materials are considered pivotal for next-generation high-performance energy storage systems.

Despite these inherent advantages, the scalable synthesis of high-quality SC-NCM cathodes faces multiple substantial challenges. Involving energy-intensive and time-consuming procedures exceeding 20 h, conventional solid-state reaction routes necessitate repeated cycles of high-temperature treatments, intermediate grinding stages, and meticulous particle size classification [16,17]. These steps not only increase manufacturing costs but also frequently introduce impurities and cause surface degradation. Moreover, the obtained particles often exhibit irregular morphology, broad size distribution, and inconsistent crystallinity, which adversely affect electrode processing and electrochemical performance [18,19]. A critical limitation further resides in the doping strategy itself: conventional powder-mixing techniques inherently struggle to attain atomic-scale uniform distribution of dopant elements. Such limitations frequently result in localized compositional heterogeneity, inadequate stabilization of the host matrix, and consequently, constrained enhancements in cycling stability and rate capability. These technical bottlenecks, in turn, impose substantial barriers to the commercial viability of SC-NCM, underscoring the urgent need for advanced doping methodologies that transcend these conventional constraints.

Recently emerging as ideal precursors for constructing well-defined functional materials, MOFs are distinguished by their periodic porous structures and atomically dispersed metal nodes. This unique structural configuration, featuring ordered porosity and precisely positioned metal centers, grants exceptional control over the spatial arrangement and compositional uniformity of active sites [20–23]. Afforded by their unique structural homogeneity and compositional tunability, unprecedented opportunities for materials design emerge. Employed as self-templates, MOFs guide the formation of uniform single-crystal particles through controlled calcination processes—a capability that underpins their transformative potential in precision material engineering [24,25]. Crucially, the molecular-level distribution inherent to metal ions within MOFs permits precise pre-incorporation of heteroelements—a mechanism that directly enables *in situ* atomic-scale doping during crystallization. This capability, challenging to replicate via conventional methodologies, highlights a transformative advantage: the spatial and temporal synchronization of dopant introduction with crystalline growth, ensuring unparalleled control over material composition and structure at the atomic level.

In this work, we demonstrate a novel MOF-mediated strategy for the one-step synthesis of *in situ* Nb⁵⁺-doped SC-NCM cathode materials (SC90-Nb). A Ni-Co-Mn-based MOF (MOF90) serves simultaneously as the precursor and self-template, guiding the oriented growth of monodisperse single-crystal particles while facilitating homogeneous Nb incorporation into the transition metal layers. At a current rate of 1C, SC90-Nb delivers a high initial discharge capacity of 176 mAh g⁻¹. More notably, it exhibits excellent capacity retention of 86.36% after 200 cycles. This approach provides new insights into the precise control of both morphology and composition for developing high-performance cathode materials.

2. Materials and Methods

2.1. Material Synthesis

2.1.1. Synthesis of MOF-90

A homogeneous solution was produced through the initial dissolution of 0.48 g of 4,4'-biphenyldicarboxylic acid—denoted as BPDC (97%, Shanghai Macklin)—in 15 mL of N,N-dimethylformamide (DMF, 98%, Shanghai Macklin), achieved via continuous stirring sustained for 10 min. Subsequent to the homogenization step, a precisely measured 2 mL aliquot of 1 M NaOH was incrementally delivered via dropwise addition into the reaction medium. The mixture underwent sustained mechanical stirring for a 2 h period to achieve complete deprotonation of the BPDC ligand, culminating in its formal designation as Solution A for subsequent synthetic utilization. The molar ratio of nickel, cobalt, and man-

ganese ions—ninety parts nickel to five parts cobalt to five parts manganese—was precisely targeted at 90:5:5 for MOF-90 synthesis. Solution B was formulated by dissolving 0.7878 g of $\text{Ni}(\text{NO}_3)_2 \cdot 6\text{H}_2\text{O}$ with 99% purity from Shanghai Macklin, 0.044 g of $\text{Co}(\text{NO}_3)_2 \cdot 6\text{H}_2\text{O}$ with 99% purity from Macklin, and 0.0537 mL of $\text{Mn}(\text{NO}_3)_2$ solution with 50% in aqueous medium from Shanghai Macklin, all in 10 mL of deionized water. Solutions A and B underwent immediate blending followed by thermal agitation at 80 °C for a 2 h interval. Through metal-ligand coordination involving deprotonated BPDC ligands and divalent metal ions, the initially clear solution exhibited a gradual phase transition—manifesting as a white emulsion formation during continuous stirring. Centrifugal separation enabled the recovery of the product, followed by sequential purification through three cycles of deionized water rinsing. This meticulous purification process culminated in the successful synthesis of MOF-90.

2.1.2. Synthesis of SC90

The as-prepared MOF-90 precursor was pre-calcined at 400 °C to obtain SC90-pre. In the subsequent synthesis phase, SC90-pre was combined with lithium hydroxide (LiOH)—sourced from Macklin with 99.5%—maintaining a stoichiometric balance precisely calibrated at 1 mole of SC90-pre to 1.05 moles of lithium source. The mixture was subjected to a conventional calcination process at 900 °C for 15 h under an oxygen atmosphere, with a heating rate of 5 °C·min⁻¹. The resulting product was thoroughly ground to obtain the final material, denoted as SC90.

2.1.3. Synthesis of SC90-Nb

SC90-Nb was synthesized following the procedure described in Section 2.1.1, with the modification that 1 mol% of C4H4NNbO9.nH2O (99.99 wt.%, Macklin) was added as the niobium source to Solution A for the preparation of the in situ Nb-doped MOF-90. The in situ Nb-doped MOF-90 was precalcined at 400 °C to obtain an intermediate product. This product was combined with lithium hydroxide (LiOH)—sourced from Macklin with 99.5 wt.%—maintaining a stoichiometric balance precisely calibrated at 1 mole of SC90-pre to 1.05 moles of lithium source. The mixture was subsequently calcined at 900 °C for 15 h under an oxygen atmosphere using a heating rate of 5 °C·min⁻¹. Finally, the resulting material was thoroughly ground to obtain the final product, denoted as SC90-Nb.

2.2. Materials Characterizations

Characterization of SC90 and SC90-Nb crystal structures employed an X-ray diffractometer (DX-2700 model) for data acquisition spanning the 2θ interval from 10° to 90°, utilizing a scanning step precision of 0.02°. Meticulous analysis of sample microstructures was conducted via high-resolution transmission electron microscopy (HRTEM), specifically employing the JEOL F200 instrument. Through scanning electron microscopy (SEM) utilizing the Regulus SU8230 instrument, the surface topographies and secondary particle dimensions of both samples were systematically investigated. Systematic investigation of elemental valence states and surface chemical composition was performed utilizing X-ray photoelectron spectroscopy (XPS) with the Thermo Scientific ESCALAB 250Xi system. Elemental distribution analysis employed energy dispersive X-ray spectroscopy (EDX) scanning to map spatial elemental patterns.

2.3. Electrochemical Measurements

The electrochemical performance assessment, specifically targeting the charge–discharge characteristics of both SC90 and SC90-Nb composite systems, was methodologically grounded in standardized CR2025 button cell testing protocols. A cathodic slurry was meticulously formulated by blending Super P, polyvinylidene fluoride (PVDF) and active

materials in an 1:1:8 proportional mass mixture, augmented with an optimized volume of N-methyl-2-pyrrolidone (NMP) solvent. The composite blend underwent uniform application onto a polished aluminum foil substrate, followed by vacuum oven treatment at 110 °C an 8 h interval to ensure complete solvent removal. Subsequent processing involved precision die-cutting into 14 mm diameter electrode discs, which were then subjected to accurate mass measurement prior to electrochemical testing. Featuring a ternary solvent matrix of ethylene carbonate (EC), diethyl carbonate (DEC), and ethyl methyl carbonate (EMC) in equimolar volumetric ratios (1:1:1), the electrolytic formulation integrated 1.0 M lithium hexafluorophosphate (LiPF_6) as the principal solute. This composition was further augmented with 1% by mass of ascorbic acid as a redox-stabilizing additive to enhance electrochemical stability. The assembly of electrochemical cells employed Celgard-2325 separator membrane and lithium metal counter electrode within an argon-filled glovebox environment. The electrochemical performance evaluation of the assembled button cells was executed under controlled voltage-current conditions, employing the CT2001A model of the Land testing apparatus for quantitative analysis. An electrochemical interface kinetics characterization protocol was established via the CHI604e electrochemical platform. This methodology employed a 5 mV alternating current perturbation amplitude and swept the frequency domain from 0.001 Hz to 10^5 Hz, enabling comprehensive impedance spectrum analysis.

3. Results

The synthesis framework (Figure 1a) delineates a groundbreaking one-step strategy for fabricating *in situ* Nb^{5+} -doped SC-NCM. The process commences with solvothermal synthesis of a Ni-Co-Mn MOF, which serves dual roles as both precursor and self-template. Through precise ligand coordination chemistry, pentavalent niobium ions (Nb^{5+}) are pre-anchored within the MOF framework, enabling atomic-level homogeneity during subsequent crystallization. Controlled thermal treatment pathways are then implemented to guide oriented nucleation and anisotropic growth of high-density single-crystal particles. The MOF-90 exhibits a well-defined blade-like morphology with uniform nanoscale dimensions precisely measured at 3 μm in length and 0.5 μm in width, as demonstrated in Figure 1b–d. This distinctive shape arises from a coordinated self-assembly process mediated by precisely regulated synthesis parameters, including controlled deprotonation of organic linkers and optimized thermal treatment pathways. The sharp edges and smooth surfaces of the blades suggest a high crystallinity and low defect density. The unequivocal demonstration of successful BPDC ligand coordination within MOF-90 is conclusively established through X-ray diffraction (XRD) analysis (Figure 1f), a structural verification that highlights the precision of MOF-mediated coordination chemistry [26–28]. Figure 1e reveals that the pre-calcined SC90-pre exhibits uniformly distributed nanoscale aggregates with dimensions precisely controlled at approximately 500 nm. XRD analysis, as visualized in the accompanying spectrogram (Figure 1g), confirms the crystalline phase as nickel(II) oxide (NiO) with JCPDS card No. 44-1159. The diffraction pattern displays sharp peaks at 37.2°, 43.3°, and 62.9°, corresponding to the (101), (012), and (110) crystallographic planes.

The chemical compositions of the synthesized SC90 and SC90-Nb samples were determined via ICP-OES analysis, with the results presented in Table 1. These findings show close agreement with the intended compositions, confirming the successful synthesis of SC90 with a Ni:Co:Mn ratio of 90:5:5 and SC90-Nb retaining nearly identical base metal proportions ($\text{Ni:Co:Mn} \approx 90:5:5$), while incorporating approximately 1% Nb by atomic content. This consistency validates both the precision of the synthesis protocol and the targeted stoichiometric control.

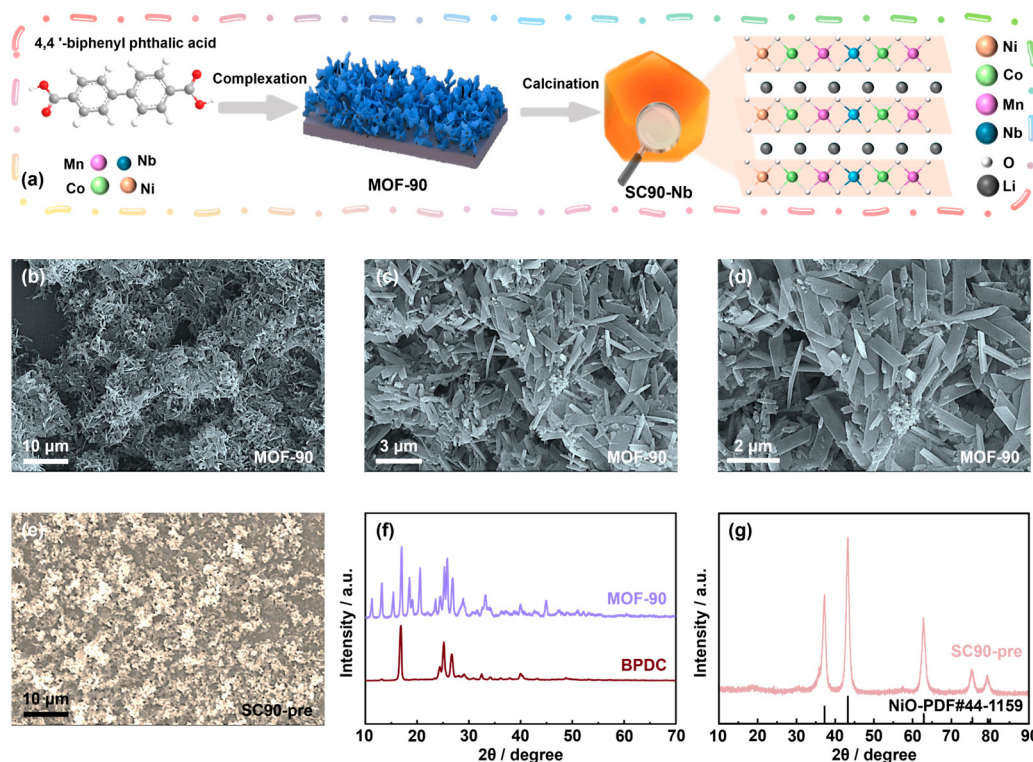


Figure 1. (a) Synthesis pathway diagram for advanced material SC90-Nb, (b–d) SEM image of MOF-90, (e) SEM image of SC90-pre, (f) XRD pattern of MOF-90 and BPDC, and (g) XRD pattern of SC90-pre.

Table 1. ICP-OES Spectrometric Evaluation of SC90 and SC90-Nb.

Sample	Chemical Composition (at. %)				
	Li	Ni	Co	Mn	Nb
SC90	1.071	0.902	0.047	0.051	0
SC90-Nb	1.066	0.892	0.049	0.050	0.009

Figure 2a,b presents a comparative morphological assessment of single-crystal particles, revealing that both SC90 and SC90-Nb samples exhibit monodisperse architectures with dimensions precisely controlled at 1.16 μm and 0.79 μm , respectively. This is further supported by Figure S1, which visually demonstrates the particle size distribution and morphological uniformity achieved through doping. The statistically significant reduction in particle size ($\Delta d \approx 0.37 \mu\text{m}$) for the Nb-doped SC90-Nb variant provides unequivocal evidence of Nb^{5+} -induced dimensional tuning. Specifically, Nb^{5+} incorporation modulates surface energy anisotropy and lattice strain during the nucleation-growth process. By reducing the driving force for lateral grain growth while promoting axial elongation, Nb doping results in smaller yet more geometrically uniform particles. The electrochemical advantages of this optimized morphology are manifold. Smaller particle size shortens Li^+ diffusion pathways, enhancing rate capability and reducing polarization. Uniform particle geometry mitigates mechanical stress accumulation during cycling, improving structural stability (Figure 2e).

The exceptional fidelity of the layered hexagonal $\alpha\text{-NaFeO}_2$ crystal framework (space group $R\text{-}3m$) under Nb^{5+} incorporation is conclusively verified through Rietveld refinement, with reliability factors (R_{wp}) consistently below 10% across all specimens (Figure 2c,d and Table 2). Characteristic splitting of the (006)/(102) and (108)/(110) diffraction doublets provides unambiguous evidence of ordered layer formation, corroborating minimal

stacking faults and high crystallographic order. Both pristine SC90 and niobium-modified SC90-Nb maintain c/a ratios exceeding 4.8—a critical threshold for preserving the layer architecture essential for rapid Li^+ transport. Conclusively established through extensive characterization, nickel-rich cathode materials exhibit an intrinsic propensity toward $\text{Li}^+/\text{Ni}^{2+}$ cation mixing—a deleterious phenomenon that fundamentally compromises electrochemical performance metrics. The intensity ratio of diffraction peaks (I_{003}/I_{104}) has emerged as a universally recognized metric for quantifying this disorder, with values exceeding 1.2 empirically delineating minimal mixing regimes. Quantitative diffraction analysis reveals striking differential behavior between specimens: the pristine SC90 exhibits an I_{003}/I_{104} ratio of 1.23, signifying moderate mixing, while niobium-modified SC90-Nb demonstrates a substantial elevation to 1.39—surpassing the critical threshold and confirming pronounced suppression of $\text{Li}^+/\text{Ni}^{2+}$ disorder.

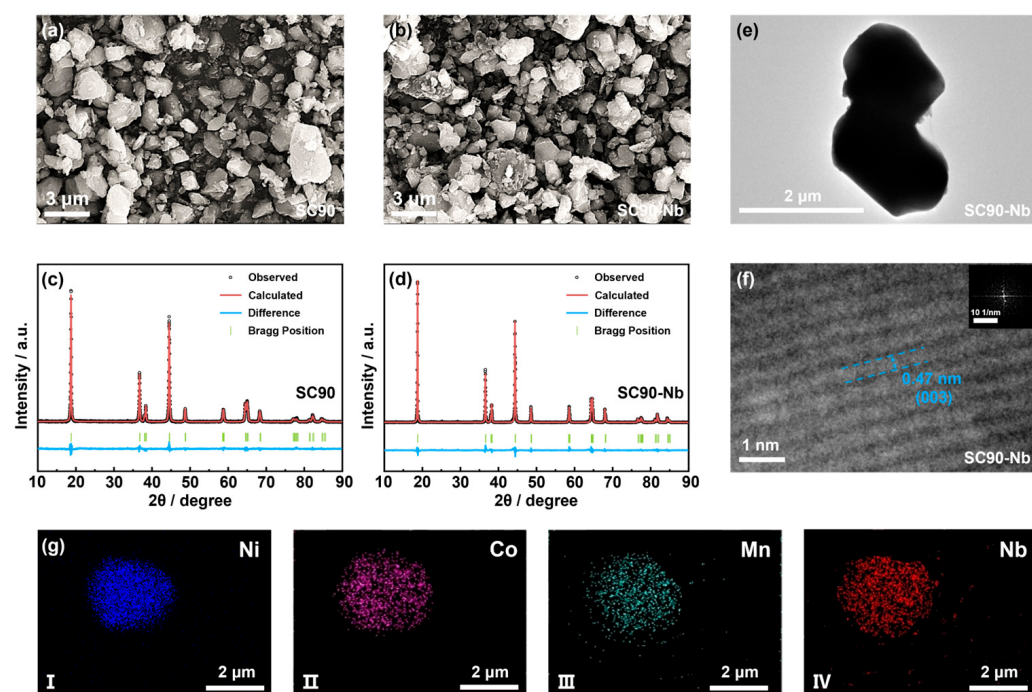


Figure 2. SEM image of (a) SC90 and (b) SC90-Nb, XRD refinement pattern of (c) SC90 and (d) SC90-Nb, (e) TEM image of SC90-Nb, (f) HRTEM image of SC90-Nb and SAED patterns (inset), and (g) Elemental mapping images of SC90-Nb: (I) Ni, (II) Co, (III) Mn, (IV) Nb.

Table 2. Refined lattice parameters of SC90 and 2% LNO@NCM samples.

Sample	a (Å)	c (Å)	V (Å 3)	c/a	I_{003}/I_{104}	Rwp (%)
SC90	2.8723	14.1961	101.43	4.9424	1.23	7.28%
SC90-Nb	2.8726	14.1957	101.45	4.9418	1.39	6.64%

HRTEM unveils that SC90-Nb adopts a pristine layered architecture with precisely measured interlayer spacing of 0.47 nm, aligning unambiguously with the (003) crystallographic plane (Figure 2f), with selected area electron diffraction (SAED) patterns exhibiting sharp diffraction spots indicative of minimal defect density (inset in Figure 2f). Energy-dispersive X-ray spectroscopy (EDX) elemental mapping provides definitive evidence of homogeneous Nb $^{5+}$ incorporation, with nanoscale line scan analysis revealing uniform intensity profiles across the particle diameter (Figure 2g).

X-ray photoelectron spectroscopy (XPS) surveys (Figure 3a,b) conclusively confirm the presence of Ni, Co, Mn, O, and trace Nb elements, establishing successful Nb^{5+} incorporation while preserving surface integrity. Quantitative peak deconvolution of the Ni 2p spectra (Figure 3c,d) reveals distinct peak positions: for SC90-Nb, the Ni $2\text{p}_{3/2}$ Ni^{3+} peak appears at 856.29 eV (compared to 856.26 eV in pristine SC90) and the Ni^{2+} peak at 855.00 eV (compared to 854.96 eV in SC90), demonstrating unambiguous spectral resolution. Furthermore, the $\text{Ni}^{3+}/\text{Ni}^{2+}$ ratio exhibits a dramatic increase from 1.05 in the pristine SC90 to 1.99 in Nb-doped SC90-Nb (Figure 3g), indicating significant stabilization of the Ni^{3+} oxidation state. This differential oxidation behavior, quantified through area ratio calculations, underscores Nb^{5+} 's electron-modulating effect on local electron density, which suppresses detrimental Ni^{2+} reduction and enhances redox activity. O 1s spectra exhibit a characteristic adsorption peak at 531.54 eV, confirms that Nb-SC90 exhibits 18.0% lattice oxygen content (vs. 15.9% in SC90) (Figure 3e,f). This oxygen immobilization directly facilitates Ni^{2+} to Ni^{3+} oxidation by stabilizing the lattice oxygen frame-work. As demonstrated in Figure 3h,i, the Nb 3d peak was exclusively observed in the SC90-Nb sample. Specifically, the binding energies of Nb $3\text{d}_{3/2}$ and Nb $3\text{d}_{5/2}$ in SC90-Nb were measured at 209.08 eV and 206.33 eV, respectively, aligning precisely with the characteristic binding energy values of Nb^{5+} oxidation state. This consistency further confirms the presence of pentavalent niobium species in the sample.

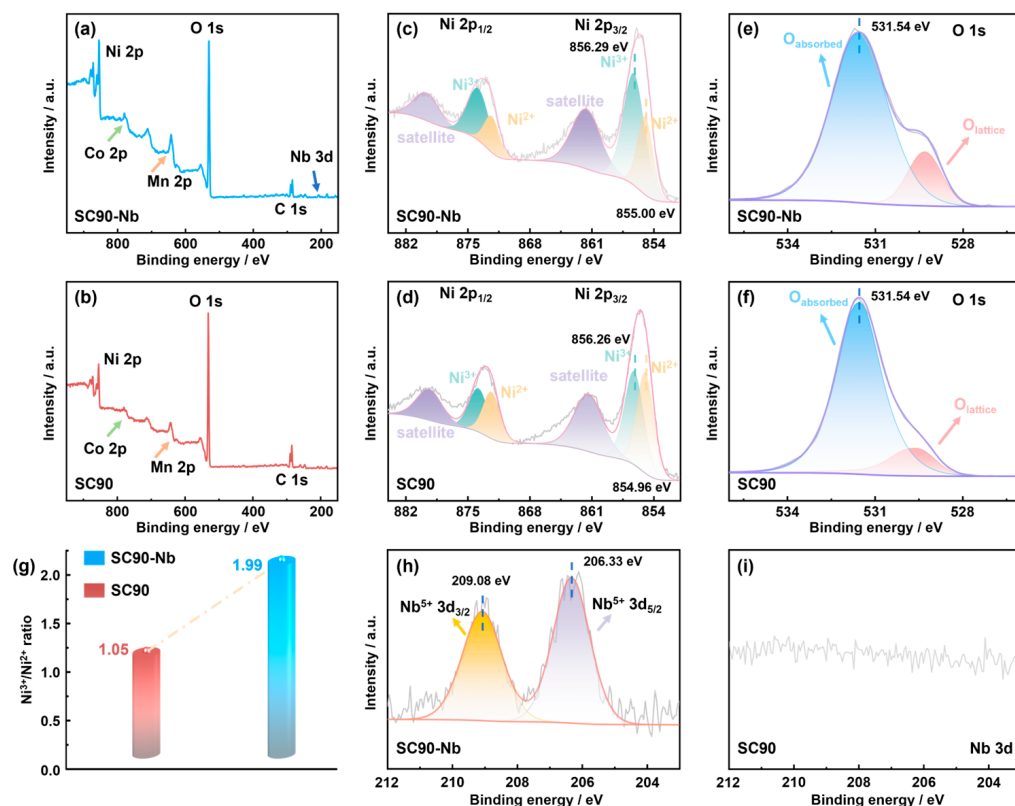


Figure 3. XPS spectra of (a) SC90-Nb and (b) SC90, Ni 2p XPS spectra of (c) SC90-Nb and (d) SC90, O 1s XPS spectra of (e) SC90-Nb and (f) SC90, (g) $\text{Ni}^{3+}/\text{Ni}^{2+}$ ratio of SC90 and SC90-Nb, and Nb 3d XPS spectra of (h) SC90-Nb and (i) SC90.

To elucidate the impact of Nb doping on electrochemical performance, comprehensive characterization was conducted. Upon completing 200 charge/discharge cycles (Figure 4a), the SC90-Nb variant distinctly outperforms its pristine counterpart: it achieves an exceptional initial discharge capacity of 176 mAh/g and maintains a remarkable capacity retention of 86.36%, whereas pristine SC90 records a lower initial capacity of 163 mAh/g

and a drastic decline to 21.53% retention. Rate performance evaluation reveals the exceptional electrochemical performance of SC90-Nb under high-current conditions. Even at 5C discharge rate, the Nb-doped variant maintains a discharge capacity of 157.7 mAh/g, significantly exceeding the 143.3 mAh/g delivered by pristine SC90 under identical testing protocols (Figure 4b). As demonstrated in Figure 4c, the SC90-Nb electrode exhibits an initial discharge capacity of 204.4 mAh/g, marginally surpassing the 202.7 mAh/g measured for the pristine SC90 cathode under identical testing conditions (0.1C discharge rate, 2.75–4.3V voltage window). The result demonstrates that *in situ* niobium doping maintains comparable electrochemical performance to the undoped counterpart while potentially enhancing structural stability or cycle life. Comparative evaluation of discharge trajectories reveals distinctive voltage stability characteristics among the two electrode systems. The pristine SC90 exhibits substantial voltage decay with increasing cycle numbers, indicative of progressive degradation in electrochemical reversibility. In contrast, the Nb-doped SC90-Nb variant demonstrates only marginal voltage degradation, maintaining superior discharge voltage retention throughout the cycling protocol. This differential behavior—attributable to optimized Nb⁵⁺-induced electronic modulation and refined crystal architecture—translates to enhanced operational durability and reduced capacity fade rates. Quantitative analysis of voltage-cycle trajectories (Figure 4d,e) confirms the synergistic relationship between compositional engineering and electrochemical stability, establishing SC90-Nb as a superior candidate for next-generation high-energy-density battery systems. The SC90-Nb sample demonstrates remarkable electrochemical resilience, maintaining a reversible capacity of 160.8 mAh g⁻¹ after 100 cycles at 1C—corresponding to an impressive 91.4% capacity retention. In stark contrast, the pristine SC90 sample exhibits a markedly lower retention rate of only 47.7% under identical conditions. When contextualized against relevant literature benchmarks (Figure S2), SC90-Nb's performance profile stands out as exceptionally competitive, showcasing superior long-term stability while maintaining practical initial capacity metrics [29–36].

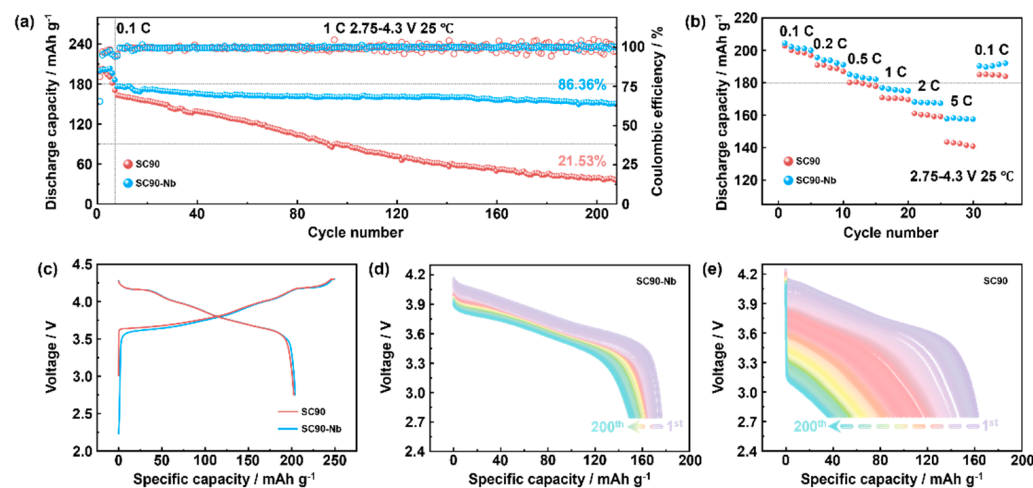


Figure 4. (a) Comparative Cycling Stability Analysis at 1C Rate (2.75–4.30 V) for SC90 and Nb-SC90 Cathodes, (b) Comparative Rate Capability Assessment of SC90 and SC90-Nb electrode systems, (c) Comparative electrochemical signature analysis of initial charge–discharge profiles for SC90 and Nb-SC90 electrodes, and Electrochemical degradation analysis of discharge profiles for (d) SC90-Nb and (e) SC90 electrodes under progressive 1C cycling.

Systematic electrochemical impedance analysis was meticulously executed on SC90 and SC90-Nb cathode systems following three-cycle activation and extended 100-cycle cycling protocols, enabling the precise quantification of Li⁺ transport dynamics. The Nyquist impedance profiles exhibit distinctive semicircular signatures: the primary mid-

frequency arc delineates CEI film resistance (R_f), while the secondary low-frequency arc quantifies charge transfer resistance (R_{ct}) at the NCM-electrolyte interface. Quantitative impedance parameters, rigorously validated through equivalent circuit modeling (inset in Figure 5) and derived from EIS measurements (Figure 5a–d and Table 3), reveal a marked reduction in R_{ct} values for SC90-Nb compared to pristine SC90 after 100 cycles. This kinetic enhancement—attributable to Nb⁵⁺ doping-mediated electronic modulation—facilitates accelerated Li⁺ diffusion and diminished interfacial polarization, as evidenced by superior rate capability and extended cycle life.

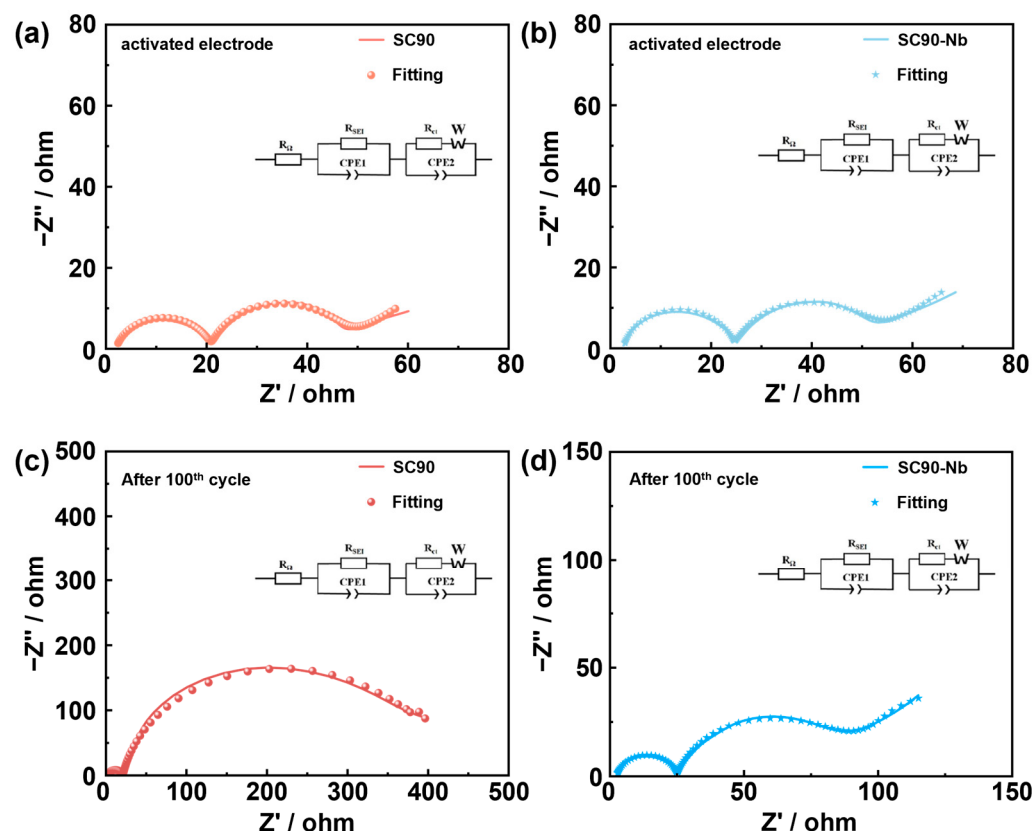


Figure 5. Nyquist impedance analysis of (a) SC90 and (b) SC90-Nb after three cycles of activation, along with Nyquist impedance analysis of (c) SC90 and (d) SC90-Nb after 100th cycle.

Table 3. EIS fitting metrics for SC90 and SC90-Nb Cathodes Following Three-Cycle Activation and 100th-Cycle Evaluation.

Sample	Three-Cycle Activation		After 100-Cycle	
	R_f (Ω)	R_{ct} (Ω)	R_f (Ω)	R_{ct} (Ω)
SC90	18.44	29.09	18.92	376.31
SC90-Nb	21.93	30.02	22.58	64.16

4. Conclusions

In this study, we pioneer a groundbreaking paradigm by introducing an innovative one-pot synthesis strategy mediated by metal/organic frameworks (MOFs) to achieve precise structural control and *in situ* Nb⁵⁺ doping within single-crystal SC-NCM electrodes. This methodology strategically harnesses MOF chemistry to synchronize morphological tuning with homogeneous niobium incorporation, thereby simultaneously achieving enhanced structural precision and optimized electrochemical performance while preserving material integrity. Notably, the SC90-Nb electrode demonstrates exceptional cycle

stability with 86.36% capacity retention after 200 cycles, outperforming pristine materials. Its superior cycle life and reduced capacity fading rate position it as a promising candidate for applications requiring prolonged operational longevity over raw capacity metrics. This holistic innovation—spanning synthesis optimization to performance enhancement—provides critical insights for industrializing next-generation safe, durable lithium-ion batteries, showcasing unprecedented control over electrochemical stability and energy density. The integration of MOF-mediated synthesis with targeted dopant engineering offers a transformative pathway for advancing high-performance electrode materials with scalable manufacturing potential.

Supplementary Materials: The following supporting information can be downloaded at <https://www.mdpi.com/article/10.3390/batteries11100368/s1>, Figure S1. Histogram of particle size statistics: (a) SC90-Nb and (b) SC90. Figure S2. Comparison of the cycling stability of SC90-Nb cathode and other nickel-rich cathodes after 100 cycles.

Author Contributions: Conceptualization, writing and investigation, Y.G.; review and editing H.Z.; Software, S.L., S.G. and M.L.; resources, funding acquisition, project administration, X.L., Y.Z. and P.G. All authors have read and agreed to the published version of the manuscript.

Funding: The present investigation acknowledges financial backing from three distinct funding sources: the Shandong Natural Science Foundation Youth Fund (Grant No. ZR2023QB230), the Double First-Class Discipline Construction Fund Project at Harbin Institute of Technology Weihai Campus (Contract No. 2023SYLHY11) and the National Natural Science Foundation (Award No. 22309035).

Data Availability Statement: The original contributions presented in this study are included in the article/Supplementary Materials. Further inquiries can be directed to the corresponding author.

Conflicts of Interest: The authors declare no conflict of interest.

References

1. Armand, M.; Tarascon, J.M. Building Better Batteries. *Nature* **2008**, *451*, 652–657. [[CrossRef](#)]
2. Li, W.; Erickson, E.M.; Manthiram, A. High-Nickel Layered Oxide Cathodes for Lithium-Based Automotive Batteries. *Nat. Energy* **2020**, *5*, 26–34. [[CrossRef](#)]
3. Zhou, H.; Zhang, C.; Gong, S.; Sun, Y.; Guan, S.; Gao, Y.; Gao, P.; Zhu, Y.; Lou, S.; Li, X. Electroless Plating Engineering Triggered Shielding Effect Enables Stable Nickel-Rich Cathode for High-Energy-Density Lithium-Ion Batteries. *J. Colloid Interface Sci.* **2025**, *698*, 138129. [[CrossRef](#)]
4. Kim, U.-H.; Jun, D.-W.; Park, K.-J.; Zhang, Q.; Kaghazchi, P.; Aurbach, D.; Major, D.T.; Goobes, G.; Dixit, M.; Leifer, N.; et al. Pushing the Limit of Layered Transition Metal Oxide Cathodes for High-Energy Density Rechargeable Li Ion Batteries. *Energy Environ. Sci.* **2018**, *11*, 1271–1279. [[CrossRef](#)]
5. Jiang, M.; Danilov, D.L.; Eichel, R.; Notten, P.H.L. A Review of Degradation Mechanisms and Recent Achievements for Ni-Rich Cathode-Based Li-Ion Batteries. *Adv. Energy Mater.* **2021**, *11*, 2103005. [[CrossRef](#)]
6. Kim, U.-H.; Kuo, L.-Y.; Kaghazchi, P.; Yoon, C.S.; Sun, Y.-K. Quaternary Layered Ni-Rich NCMA Cathode for Lithium-Ion Batteries. *ACS Energy Lett.* **2019**, *4*, 576–582. [[CrossRef](#)]
7. Zhou, H.; Xin, F.; Pei, B.; Whittingham, M.S. What Limits the Capacity of Layered Oxide Cathodes in Lithium Batteries? *ACS Energy Lett.* **2019**, *4*, 1902–1906. [[CrossRef](#)]
8. Lu, J.; Xu, C.; Dose, W.; Dey, S.; Wang, X.; Wu, Y.; Li, D.; Ci, L. Microstructures of Layered Ni-Rich Cathodes for Lithium-Ion Batteries. *Chem. Soc. Rev.* **2024**, *53*, 4707–4740. [[CrossRef](#)] [[PubMed](#)]
9. Han, G.-M.; Kim, Y.-S.; Ryu, H.-H.; Sun, Y.-K.; Yoon, C.S. Structural Stability of Single-Crystalline Ni-Rich Layered Cathode upon Delithiation. *ACS Energy Lett.* **2022**, *7*, 2919–2926. [[CrossRef](#)]
10. Tang, W.; Shu, Z.; Li, A.; Huang, X.; Li, W. Enhancing Structural Integrity and Long-Term Cycling Stability of High-Voltage Single-Crystalline Ni-Rich Cathodes via Surface/Subsurface Dual-Functional Modification Engineering. *Energy Storage Mater.* **2025**, *77*, 104185. [[CrossRef](#)]
11. Lu, Z.; Yang, H.; Sun, J.; Okagaki, J.; Choe, Y.; Yoo, E. Conformational Isomerism Breaks the Electrolyte Solubility Limit and Stabilizes 4.9 V Ni-Rich Layered Cathodes. *Nat. Commun.* **2024**, *15*, 9108. [[CrossRef](#)]

12. Ni, L.; Zhang, S.; Di, A.; Deng, W.; Zou, G.; Hou, H.; Ji, X. Challenges and Strategies towards Single-Crystalline Ni-Rich Layered Cathodes. *Adv. Energy Mater.* **2022**, *12*, 2201510. [[CrossRef](#)]
13. Zhang, H.; He, X.; Chen, Z.; Yang, Y.; Xu, H.; Wang, L.; He, X. Single-Crystalline Ni-Rich $\text{LiNi}_x\text{Mn}_y\text{Co}_{1-x-y}\text{O}_2$ Cathode Materials: A Perspective. *Adv. Energy Mater.* **2022**, *12*, 2202022. [[CrossRef](#)]
14. Tan, Z.; Chen, X.; Lin, J.; Huang, Y.; Cheng, W.; Liu, Q.; Zhang, H.; Ren, F.; Huang, Y.; Liu, Z.; et al. Restraining Planar Gliding in Single-Crystalline $\text{LiNi}_{0.9}\text{Co}_{0.05}\text{Mn}_{0.05}\text{O}_2$ Cathodes by Combining Bulk and Surface Modification Strategies. *Angew. Chem. Int. Ed.* **2025**, *64*, e202419903. [[CrossRef](#)] [[PubMed](#)]
15. Zou, Y.; Yu, D.; Tang, Y.; Yan, Y.; Qiao, Y.; Bao, J.; Sun, S.-G. The Dilemma of Single-Crystal High-Nickel $\text{LiNi}_x\text{Co}_y\text{Mn}_{1-x-y}\text{O}_2$ ($x \geq 0.9$) Cathodes: Inhomogeneous Delithiation inside and Outside the Particle. *Chem. Eng. J.* **2025**, *504*, 158800. [[CrossRef](#)]
16. Huang, H.; Zhu, H.; Gao, J.; Wang, J.; Shao, M.; Zhou, W. Grain-growth Inhibitor with Three-section-sintering for Highly Dispersed Single-crystal NCM90 Cubes. *Angew. Chem.* **2024**, *136*, e202314457. [[CrossRef](#)]
17. Zhou, W.; Huang, H.; Liu, X.; Gao, J.; Hao, S.; Yang, Y.; Qiu, J. Perspective on the Preparation Methods of Single Crystalline High Nickel Oxide Cathode Materials. *Adv. Energy Mater.* **2023**, *13*, 2300378. [[CrossRef](#)]
18. Qian, G.; Zhang, Y.; Li, L.; Zhang, R.; Xu, J.; Cheng, Z.; Xie, S.; Wang, H.; Rao, Q.; He, Y.; et al. Single-Crystal Nickel-Rich Layered-Oxide Battery Cathode Materials: Synthesis, Electrochemistry, and Intra-Granular Fracture. *Energy Storage Mater.* **2020**, *27*, 140–149. [[CrossRef](#)]
19. Van Den Bergh, W.; Karger, L.; Murugan, S.; Janek, J.; Kondrakov, A.; Brezesinski, T. Single Crystal Layered Oxide Cathodes: The Relationship between Particle Size, Rate Capability, and Stability. *ChemElectroChem* **2023**, *10*, e202300165. [[CrossRef](#)]
20. Yin, C.; Bao, Z.; Tan, H.; Zhou, H.; Li, J. Metal-Organic Framework-Mediated Synthesis of $\text{LiNi}_{0.5}\text{Mn}_{1.5}\text{O}_4$: Tuning the Mn^{3+} Content and Electrochemical Performance by Organic Ligands. *Chem. Eng. J.* **2019**, *372*, 408–419. [[CrossRef](#)]
21. Yin, C.; Zhou, H.; Yang, Z.; Li, J. Synthesis and Electrochemical Properties of $\text{LiNi}_{0.5}\text{Mn}_{1.5}\text{O}_4$ for Li-Ion Batteries by the Metal-Organic Framework Method. *ACS Appl. Mater. Interfaces* **2018**, *10*, 13625–13634. [[CrossRef](#)]
22. Li, T.; Bai, Y.; Wang, Y.; Xu, H.; Jin, H. Advances in Transition-Metal (Zn, Mn, Cu)-Based MOFs and Their Derivatives for Anode of Lithium-Ion Batteries. *Coord. Chem. Rev.* **2020**, *410*, 213221. [[CrossRef](#)]
23. Kong, L.; Liu, M.; Huang, H.; Xu, Y.; Bu, X. Metal/Covalent-Organic Framework Based Cathodes for Metal-Ion Batteries. *Adv. Energy Mater.* **2022**, *12*, 2100172. [[CrossRef](#)]
24. Shan, R.; Lu, X.; Xu, Y.; Shen, K.; Xia, Y.; Cai, Y.; Yao, J.; Mao, Q.; Wang, Y.; Ji, T. A Ternary MOF Derived Single Crystalline $\text{LiNi}_{1/3}\text{Mn}_{1/3}\text{Co}_{1/3}\text{O}_2$ as High-Voltage Cathodes for Lithium-Ion Batteries. *Chem. Eng. Sci.* **2023**, *268*, 118416. [[CrossRef](#)]
25. Han, X.; Meng, Q.; Sun, T.; Sun, J. Preparation and Electrochemical Characterization of Single-Crystalline Spherical $\text{LiNi}_{1/3}\text{Co}_{1/3}\text{Mn}_{1/3}\text{O}_2$ Powders Cathode Material for Li-Ion Batteries. *J. Power Sources* **2010**, *195*, 3047–3052. [[CrossRef](#)]
26. Rawool, C.R.; Karna, S.P.; Srivastava, A.K. Enhancing the Supercapacitive Performance of Nickel Based Metal Organic Framework-Carbon Nanofibers Composite by Changing the Ligands. *Electrochim. Acta* **2019**, *294*, 345–356. [[CrossRef](#)]
27. He, F.; Yang, N.; Li, K.; Wang, X.; Cong, S.; Zhang, L.; Xiong, S.; Zhou, A. Hydrothermal Synthesis of Ni-Based Metal Organic Frameworks/Graphene Oxide Composites as Supercapacitor Electrode Materials. *J. Mater. Res.* **2020**, *35*, 1439–1450. [[CrossRef](#)]
28. Zhang, W.; Yin, H.; Yu, Z.; Jia, X.; Liang, J.; Li, G.; Li, Y.; Wang, K. Facile Synthesis of 4,4'-Biphenyl Dicarboxylic Acid-Based Nickel Metal Organic Frameworks with a Tunable Pore Size towards High-Performance Supercapacitors. *Nanomaterials* **2022**, *12*, 2062. [[CrossRef](#)] [[PubMed](#)]
29. Zhu, C.; Cao, M.; Zhang, H.; Lv, G.; Zhang, J.; Meng, Y.; Shu, C.; Fan, W.; Zuo, M.; Xiang, W.; et al. Synergistic Effect of Microstructure Engineering and Local Crystal Structure Tuning to Improve the Cycling Stability of Ni-Rich Cathodes. *ACS Appl. Mater. Interfaces* **2021**, *13*, 48720–48729. [[CrossRef](#)]
30. Zhang, J.; Wang, S.; Yang, X.; Liu, Y.; Wu, Z.; Li, H.; Indris, S.; Ehrenberg, H.; Hua, W. Unravelling the Peculiar Role of Co and Al in Highly Ni-Rich Layered Oxide Cathode Materials. *Chem. Eng. J.* **2024**, *484*, 149599. [[CrossRef](#)]
31. Zuo, J.; Wang, J.; Duan, R.; Bai, Y.; Xu, K.; Zhang, K.; Wang, J.; Zhang, K.; Yang, Z.; Yang, Z.; et al. Grain Binding Derived Reinforced Interfacial Mechanical Behavior of Ni-Rich Layered Cathode Materials. *Nano Energy* **2024**, *121*, 109214. [[CrossRef](#)]
32. Jiao, T.; Liu, G.; Zou, Y.; Yang, X.; Zhang, X.; Fu, A.; Zheng, J.; Yang, Y. A Novel Trimethylsilyl 2-(Fluorosulfonyl)Difluoroacetate Additive for Stabilizing the Ni-Rich $\text{LiNi}_{0.9}\text{Co}_{0.05}\text{Mn}_{0.05}\text{O}_2$ /Electrolyte Interface. *J. Power Sources* **2021**, *515*, 230618. [[CrossRef](#)]
33. Sheng, H.; Meng, X.; Xiao, D.; Fan, M.; Chen, W.; Wan, J.; Tang, J.; Zou, Y.; Wang, F.; Wen, R.; et al. An Air-Stable High-Nickel Cathode with Reinforced Electrochemical Performance Enabled by Convertible Amorphous Li_2CO_3 Modification. *Adv. Mater.* **2022**, *34*, 2108947. [[CrossRef](#)]
34. Park, G.-T.; Namkoong, B.; Kim, S.-B.; Liu, J.; Yoon, C.S.; Sun, Y.-K. Introducing High-Valence Elements into Cobalt-Free Layered Cathodes for Practical Lithium-Ion Batteries. *Nat. Energy* **2022**, *7*, 946–954. [[CrossRef](#)]

35. Wang, W.; Zhou, Y.; Zhang, B.; Huang, W.; Cheng, L.; Wang, J.; He, X.; Yu, L.; Xiao, Z.; Wen, J.; et al. Optimized In Situ Doping Strategy Stabilizing Single-Crystal Ultrahigh-Nickel Layered Cathode Materials. *ACS Nano* **2024**, *18*, 8002–8016. [[CrossRef](#)]
36. Qian, R.; Liu, Y.; Cheng, T.; Li, P.; Chen, R.; Lyu, Y.; Guo, B. Enhanced Surface Chemical and Structural Stability of Ni-Rich Cathode Materials by Synchronous Lithium-Ion Conductor Coating for Lithium-Ion Batteries. *ACS Appl. Mater. Interfaces* **2020**, *12*, 13813–13823. [[CrossRef](#)] [[PubMed](#)]

Disclaimer/Publisher’s Note: The statements, opinions and data contained in all publications are solely those of the individual author(s) and contributor(s) and not of MDPI and/or the editor(s). MDPI and/or the editor(s) disclaim responsibility for any injury to people or property resulting from any ideas, methods, instructions or products referred to in the content.